Article

Chain entanglement enhanced strong and tough wool keratin/albumin fibers for bioabsorbable and immunocompatible surgical sutures

Haonan He[1,2,5], Xianchi Zhou [1,5], Yuxian Lai[1], Rouye Wang[1], Hongye Hao[1,2], Xintian Shen[1], Peng Zhang [1,2,3] ✉ & Jian Ji [1,2,3,4] ✉

High-performance fibers derived from non-silk proteins have garnered significant interest in biomedical applications because of their high accessibility and biocompatibility. Nonetheless, considerable challenges persist in addressing their structural defects to fabricate fibers with an optimal balance of strength and toughness. Herein, an entanglement-reinforced strategy is proposed to reconstruct high-performance non-silk protein fibers. Regenerated keratin and bovine serum albumin (BSA) are unfolded by denaturant and complementarily composited, leveraging their intrinsic cysteine re-oxidation to generate a robust mechanical cross-linking network without the requirement of an external crosslinker. The resulting drawn keratin/BSA composite fiber (DKBF) exhibits balanced mechanical performances with a breaking strength of approximately 250 MPa and a toughness of around 70 MJ m^{-3}, outperforming that of reported regenerated keratin fibers and comparable to many natural or artificial silk fibers. Additionally, DKBFs demonstrate redox-responsive mechanical behavior and hydration-induced reversible shape memory. The DKBFs show good suturing capability for wound repair in female animal models due to their excellent bioabsorbability and immunocompatibility. This work offers valuable insights into addressing the current challenges in manufacturing mechanically robust and tough non-silk protein fibers, bringing hope for the development of more sustainable and versatile materials.

Protein-engineered materials, renowned for their exceptional biocompatibility and biodegradability, have captured considerable attention for their potential in fabricating fibers[1–3], adhesives[4,5], hydrogels[6], films[7,8], and scaffolds[9], for various biomedical applications.

In high-performance protein fibers, mechanical properties assume paramount importance, particularly in biomedical applications such as artificial tendons[10], surgical sutures[11,12], biological patches[1], and bioelectronics[13]. However, the inherent conflict between strength and

[1]MOE Key Laboratory of Macromolecule Synthesis and Functionalization, Department of Polymer Science and Engineering, Zhejiang University, Hangzhou, PR China. [2]International Research Center for X Polymers, International Campus, Zhejiang University, Haining, PR China. [3]State Key Laboratory of Transvascular Implantation Devices, The Second Affiliated Hospital, School of Medicine, Zhejiang University, Hangzhou, PR China. [4]Transvascular Implantation Devices Research Institute China, Hangzhou, PR China. [5]These authors contributed equally: Haonan He, Xianchi Zhou. ✉e-mail: zhangp7@zju.edu.cn; jijian@zju.edu.cn

toughness in fiber mechanics often results in mechanically unbalanced materials[14], thereby limiting their applications. In nature, protein fibers, exemplified by spider silk, exhibit exceptional strength and toughness attributable to their unique molecular architecture, featured by both hydrophobic and hydrophilic domains[15]. During fiber spinning, spidroins orchestrate the formation of well-organized supramolecular nanostructure networks, wherein self-assembled rigid crystalline β-sheets are embedded within soft amorphous matrices[16]. Although this intricate molecular arrangement renders silk both superior strength and toughness, it also results in a delayed biodegradation process for in vivo applications. For surgical sutures, the in vivo biodegradability is a critical consideration. Generally, commercially available silk sutures are classified as non-degradable or featuring a long degradation period since it takes ~2 years to complete degradation in vivo, far beyond the sixty-day cutoff set by regulatory agencies[17,18].

In contrast, non-silk proteins, lacking such refined structures and assembly processes, often encounter significant challenges in fabricating strong and tough fibers. Recent advancements in protein fiber derived from non-silk proteins, such as recombinant supercharged elastin-like proteins SELPs and SELP-fused modular proteins[1,12,19], as well as various globular proteins[3,20], have demonstrated considerable promise for biomedical applications. Nonetheless, these proteins often necessitate glutaraldehyde to couple protein chains due to their intrinsic non-fibrous structures. Although glutaraldehyde can confer a durable mechanical support network, it would raise concerns regarding biocompatibility, as residual aldehyde groups may induce cytotoxicity or inflammatory responses[21]. Furthermore, the crosslinked network may reduce in vivo degradability[22].

Wool-derived keratin attracted tremendous attention as a non-silk protein material due to its abundance and excellent biocompatibility[7,8,23]. However, fibers derived from regenerated wool keratin often exhibit high strength but low toughness[24–27]. This phenomenon can be attributed to the prevalence of α-helix structures and a high cystine content (7–13%) within keratin. The α-helix structures furnish a rigid nano-skeleton, while the robust disulfuric bonds between nano-fibrils establish a dense crosslinking network, imparting high strength but constraining the extension of nano-spiral structures during tension, thus resulting in diminished ductility and toughness. Despite attempts to enhance mechanical properties through compounding with polymers[28,29], cellulose[30–32], viscose[33], and graphene[34], these keratin-based fibers persistently manifest a mismatch between high strength and toughness.

Here, we develop a protein chain entanglement-reinforced strategy to fabricate high-performance composite fibers from keratin and albumin proteins. Chain entanglement is a topological effect arising from the inability of polymer chains to pass through each other[35], which has been demonstrated to provide significant stiffening and toughening effects for polymer and protein hydrogels[36–39]. High-concentration urea/dithiothreitol (DTT) is utilized to unfold and expand proteins in volume, thus promoting protein chain entanglement. In this context, through denaturation and subsequent secondary structure complementarity, low-cost regenerated keratin and bovine serum albumin (BSA) are spun into strong and tough composite fibers, which rely on the inherent cysteine oxidation crosslinking of the proteins without requiring external crosslinking agents. Blending keratin with BSA balanced the contents of α-helix and β-sheet structures. The resulting drawn keratin/BSA composite fibers (DKBFs) perform a breaking strength of 249.9 ± 8.3 MPa and a toughness of 69.9 ± 10.0 MJ m^{-3}, surpassing that of natural or regenerated keratin fibers, and even comparable to many silk fibers. The redox-responsive and hydration-induced mechanical behaviors of DKBFs are also explored. In addition, the DKBFs exhibit favorable biocompatibility, degradability, and immunocompatibility, demonstrating good wound closure as surgical sutures. Our exploration demonstrates the feasibility of an entanglement-reinforced strategy for tuning the protein fiber mechanics and opens an avenue for developing mechanically balanced and highly-biocompatible regenerated protein fibers.

Results

Wet-spinning preparation of keratin/BSA composite fibers

We utilize a protein chain entanglement approach to produce keratin-based fibers through wet spinning. Initially, keratin extraction from wool was achieved using a reduction solvent containing 9.8 M lithium bromide (LiBr) and 0.1 M DTT, effectively facilitating wool dissolution[40]. Subsequent refinement of wool keratin involved dialysis and freeze-drying. Sodium dodecyl sulfate-polyacrylamide gel electrophoresis of extracted keratin shows clear bands at around ~27 kDa, ~37 kDa, 40 kDa, and >180 kDa, as observed in Supplementary Fig. 1. Circular dichroism (CD) spectra analysis illustrates a predominant α-helix structure with peaks at ~208 nm and 222 nm (Supplementary Fig. 2). These findings validate the efficacy of keratin extraction and ensure the integrity of the keratin molecular backbone[7,24].

Urea, combined with DTT, serves as a critical component in preparing a mixed spinning dope comprising keratin and BSA. Here, DTT facilitates the cleavage of disulfide bonds while urea molecules permeate between the protein molecular chains, disrupting hydrogen bonds. This process initiates a transformation of both the keratin and BSA molecules into a random structure, ultimately forming a protein entanglement system enriched with a significant quantity of cysteine residues, as illustrated in Fig. 1a. The abundance of reactive thiol groups underscores their pivotal role in governing the formation of fibers and determining fiber mechanics. During the wet-spinning process depicted in Fig. 1b, entanglement-enhanced protein spinning dope is extruded from a narrow needle, where fluid-induced shear force aligns the protein chains into a coagulation (pH 2.0) consisting of 2% (w/v) H$_2$O$_2$ and 75% ethanol. Within this coagulation medium, oxidation cross-linking facilitated by H$_2$O$_2$ and protein refolding induced by acid and dehydration proceed concurrently, facilitating the transition of the fiber from solution. Remarkably, a mere 200 mg of protein yields fibers approximately 480 m in length, as shown in Fig. 1c. The scanning electron microscope (SEM) images in Fig. 1d, e show that DKBF exhibits a smooth surface and uniform diameter of around 12 µm. Moreover, the DKBF exhibits notable birefringence, as observed in the polarized optical microscope (POM) image (Fig. 1f), demonstrating a well-aligned molecular orientation. Figure 1g indicates that the DKBF can be securely knotted without compromising its elementary filament structure, confirming its flexibility and high tensile strength. The mechanical properties of keratin-based fibers under various treatments are summarized in Fig. 1h, revealing that DKBF exhibits balanced mechanical properties, with a breaking strength of 249.9 ± 8.3 MPa and a toughness of 69.9 ± 10.0 MJ m^{-3}, in stark contrast to that of pure keratin fiber (PKF) and undrawn keratin/BSA composite fiber (UKBF).

Regulation of molecular entanglement of spinning dope via protein unfolding

The entanglement of spinning dope through protein unfolding was investigated. The formation of protein chain entanglement is intricately linked to the inherent characteristics of proteins, encompassing factors such as molecular weight and structure. Achieving entanglement typically necessitates altering the structure of protein molecules, leading to their unfolding to the greatest extent possible[36]. Typically, the native structure of proteins is upheld by intramolecular disulfide bonds and various non-covalent interactions, including electrostatic, hydrophobic, and hydrogen bonding interactions[41]. Hence, to induce protein unfolding, it becomes imperative to cleave disulfide bonds with the assistance of stabilizers such as trifluoroethanol, urea, or guanidine hydrochloride, which further stabilize the unfolded protein chains[42,43]. Herein, we employed a solvent consisting of urea and DTT
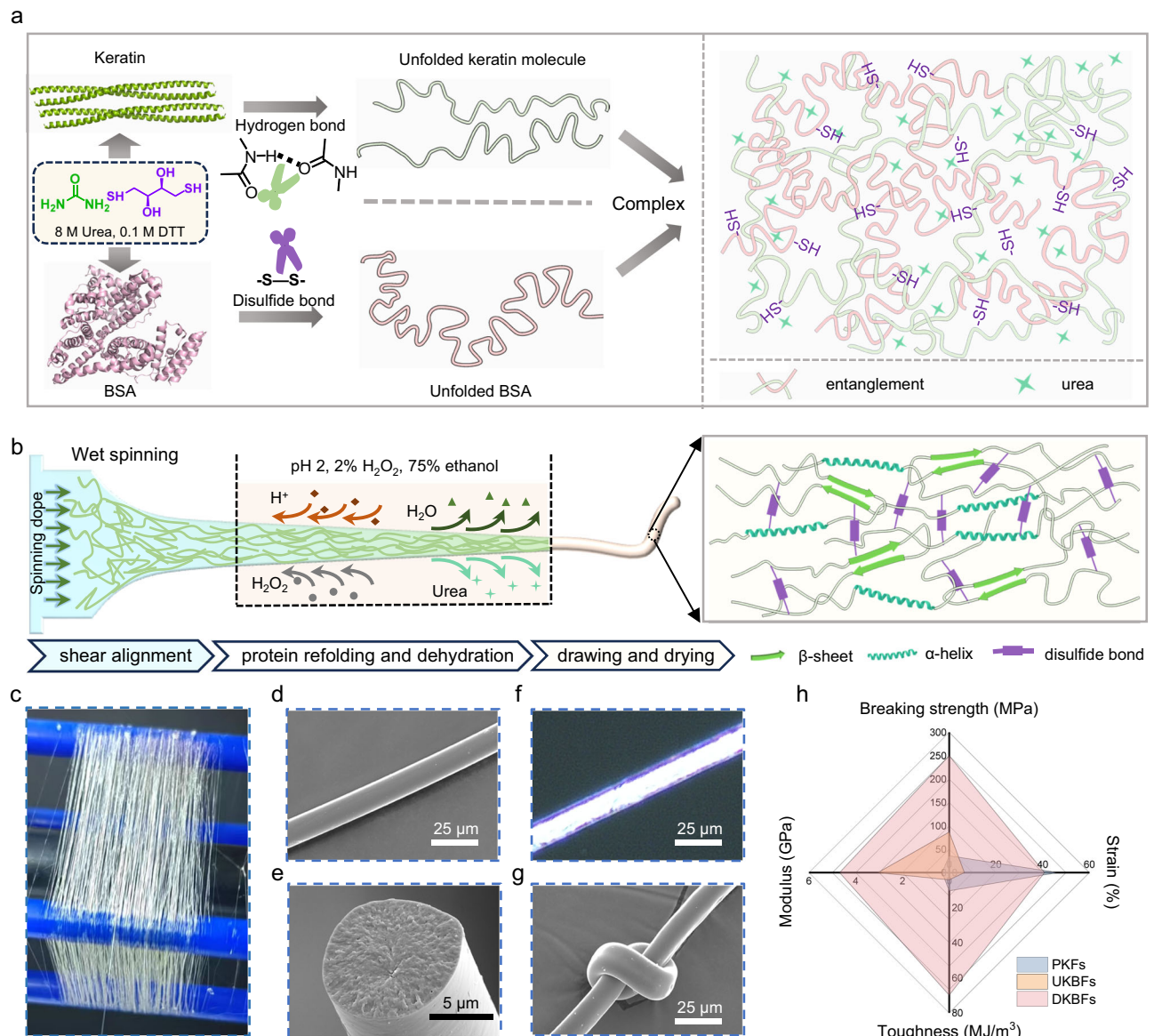
Fig. 1 | Keratin/BSA composite fiber produced using protein chain entanglement strategy. a Schematic of the protein unfolding. Urea breaks hydrogen bonds (H-bonds) while DTT cleaves disulfide bonds (S-S), leading to the unfolding of keratin from nano-aggregates into single molecules and BSA from spherical structures into random structures, respectively, thus causing protein chain entanglement in protein composite solution. **b** Schematic of the fiber formation process of the composite proteins. The unfolded proteins are aligned and squeezed into coagulation, leading to S-S crosslinking through the reoxidation of thiol groups. Simultaneously, protein refolding occurs through dehydration, followed by fiber formation through drawing collection. **c** Mass protein composite fibers are collected in a rotor collector. **d** Representative scanning electron microscopy (SEM) images of a drawn keratin/BSA composite fiber (DKBF) in longitudinal and (**e**) cross sections show a uniform diameter of ~12 µm and a smooth surface (*n* = 3). **f** A representative polarized optical microscopy (POM) image of a DKBF shows strong birefringence, indicating an ordered arrangement of proteins within the fiber (*n* = 3). **g** A SEM image of a knotted DKBF (*n* = 3). **h** A summary of the mechanical properties of keratin-based fibers under different treatments indicates that DKBFs have balanced mechanical performance. Note: PKFs denote pure keratin fibers; UKBFs denote undrawn keratin/BSA composite fibers; DKBFs denote drawn keratin/BSA composite fibers.

to dissolve proteins. For both BSA and keratin, the emission observed at 330 nm under aqueous conditions is shifted to 348 nm when adding 8 M urea and 0.1 M DTT (Supplementary Fig. 3), indicating a greater exposure of buried tryptophan residues (Trp 214) within the helical structure to the solvent during protein unfolding[44].

Molecular dynamics (MD) simulations of protein unfolding were conducted using urea to disrupt hydrogen bonding and DTT to cleave disulfide linkages (Fig. 2a). For keratin, under simulated heating conditions (90 °C) and shear forces during stirring, a progressive increase in the radius of gyration (*Rg*) and solvent-accessible surface area (SASA) was observed. Simultaneously, reductions in intramolecular hydrogen bonds (H-bonds), van der Waals (VDW) interactions, and

Coulombic energy (CE) were recorded, along with an increase in coil structure and a decrease in α-helix content, collectively indicating a gradual unfolding process (Supplementary Fig. 4). Small-angle X-ray scattering (SAXS) analysis of keratin solutions at ambient temperature revealed an *Rg* of 3.8 nm (Fig. 2b and Supplementary Table 1), signifying a transition from nanostructured aggregates to a disordered single-molecule state (Supplementary Fig. 5). Conversely, BSA dissolved readily at room temperature, exhibiting a similar unfolding trajectory but with a significantly larger equilibrium *Rg* (Supplementary Fig. 6). SAXS measurements further demonstrated an increase in the *Rg* from 2.8 nm in aqueous solution to 5.6 nm in the presence of urea/DTT (Supplementary Fig. 7). When the two proteins were mixed
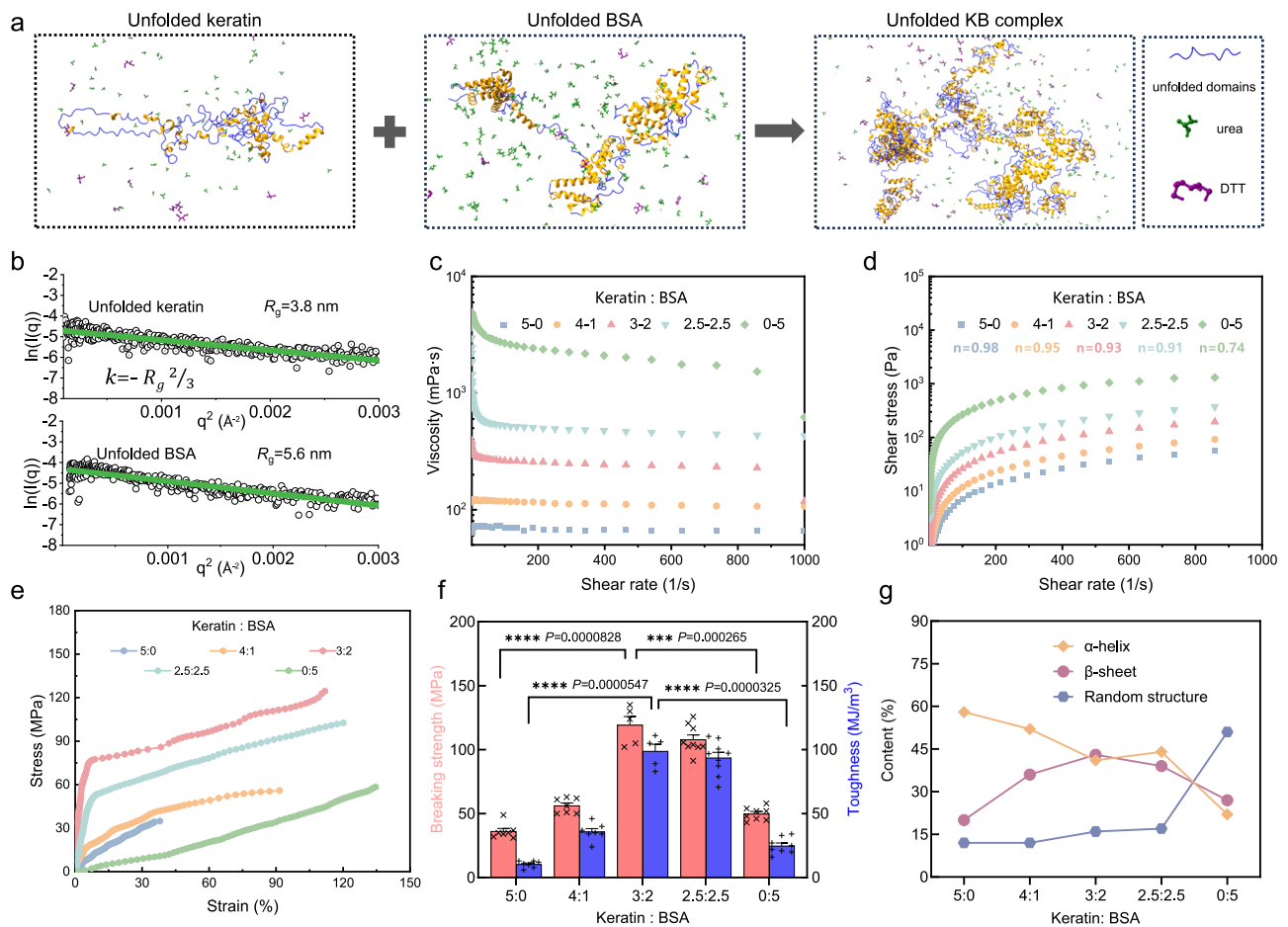
Fig. 2 | Protein unfolding and refolding regulate the mechanical properties of composite fibers. a Molecular dynamics (MD) simulations reveal that BSA and keratin undergo unfolding in the presence of urea and DTT, subsequently interacting with each other upon mixing. **b** SAXS analysis reveals R_g values of 5.6 nm and 3.8 nm for unfolded BSA and keratin, respectively. **c** Viscosity under an increasing shear rate of the protein composite solutions across varying protein ratios indicating a shear-thinning behavior. **d** The shear stress of the keratin spinning dope reveals that the non-Newtonian index gradually decreases as the proportion of BSA increases, indicating an enhancement in the entanglement within the spinning dope. **e** Representative stress-strain curves of the spun composite fibers at different protein ratios. **f** The breaking strength and toughness analysis of the spun composite fibers at different protein ratios. Data are presented as mean ± SD (5:0, $n = 7$; 4:1, $n = 7$; 3:2, $n = 5$; 2.5:2.5, $n = 9$; 0:5, $n = 8$). Statistical significance was analyzed by two-sample t-tests using OriginPro 2021 software. *ns*, no significant difference; $*p < 0.05$; $**p < 0.01$; $***p < 0.001$; $****p < 0.0001$. **g** The secondary structure content of the spun composite fibers at different protein ratios is determined through deconvolution analysis of the amide I/II region on FTIR spectra. Source data are available in the Source Data file.

under equilibrium conditions, pronounced interprotein interactions were observed. Fluctuations in the R_g indicated ongoing transitions between partial unfolding and refolding within protein structures. These conformational dynamics facilitated protein–protein collisions and subsequent entanglements (Fig. 2a). Concurrently, the increase in SASA, VDW interactions, and CE provided strong evidence of partial aggregation, further supporting the presence of intermolecular entanglements between the two proteins. Furthermore, a downward trend is observed in the coil structure, while the quantity of α-helix structures increases, suggesting the formation of new α-helix secondary structures. This transformation likely contributes to the stabilization of the entangled structure (Supplementary Fig. 8).

Subsequently, we performed a comprehensive investigation into the rheological properties of protein spinning solutions, demonstrating that DTT is essential for modulating both rheological behavior and molecular entanglement within protein systems. At 200 mg/mL, keratin exhibited limited swelling in 8 M urea and failed to achieve complete dissolution without DTT. However, the inclusion of DTT enabled full dissolution and the formation of a stable spinning solution (Supplementary Fig. 9). In contrast, BSA demonstrated distinct behavior, dissolving completely without DTT, although forming a low-viscosity solution with minimal shear-thinning properties. The addition of DTT

significantly increased the viscosity, far exceeding that of the untreated solution, underscoring the pivotal role of disulfide bond disruption in enhancing rheological properties (Supplementary Fig. 10a and Movie 1). Fiber formation experiments further confirmed the necessity of DTT for successful fiber fabrication from BSA solutions (Supplementary Movie 2).

To further elucidate the molecular entanglement, we quantified the non-Newtonian index (*n*-value) which serves as an indicator of the extent of molecular interactions and entanglement within the system, with lower *n*-values reflecting higher degrees of entanglement[45]. The DTT-treated BSA solution exhibited a significantly lower *n*-value of 0.74 compared to the 0.98 of untreated solution, highlighting enhanced molecular networking (Supplementary Fig. 10b). These demonstrated that DTT effectively disrupts disulfide bonds, thereby inducing the transition of BSA from a compact globular structure to an extended random coil conformation. This structural transformation facilitates increased molecular interpenetration and overlap, ultimately maximizing the degree of entanglement. In contrast, keratin solutions, even when treated with DTT, exhibited lower shear viscosity and higher *n*-values, indicative of weaker molecular entanglement. This behavior is likely attributable to keratin's small R_g, which inherently limits inter-molecular crosslinking and restricts the

entanglement potential of the system[36]. Therefore, we introduced highly entangled BSA solutions to modulate molecular entanglement states, demonstrating a clear trend of increasing entanglement with higher BSA content, as evidenced by a consistent decrease in n-values with increasing BSA proportions (Fig. 2c, d).

Modulation of composite fibers mechanics via balancing molecular structures

Achieving high-strength and high-toughness composite fibers requires not only optimizing molecular entanglement within the spinning solution but also precisely controlling the coagulation bath conditions to balance protein refolding and molecular networking during fiber formation. Therefore, we systematically investigated three critical parameters of the coagulation bath: pH, ethanol, and H_2O_2 content. It was observed that in a coagulation bath containing 75% ethanol and a pH of 2.0, fiber production was hindered, likely due to insufficient interactions among protein chains. Conversely, in an aqueous solution containing only H_2O_2, the extruded protein rapidly formed a gel at the outlet, blocking the channel. This gel exhibited a high proportion of random structures (Supplementary Table 2), indicating ineffective dehydration and a failure to achieve timely structural stabilization. However, when oxidation and dehydration processes occurred simultaneously during coagulation, stable fiber formation was achieved (Supplementary Movie 3). This approach enabled protein molecules to retain their entanglement while undergoing incomplete refolding and efficient dehydration, facilitating the formation of robust fibers. The influence of pH and H_2O_2 on the conformational distribution of protein molecules was further analyzed using Fourier Transform Infrared (FTIR) spectroscopy. Results revealed that excessive H_2O_2 adversely impacted the formation of β-sheet structures, likely due to the rapid establishment of oxidative cross-linking networks that impeded the transition from helix to β-sheet conformations. Additionally, an increase in hydrogen ion concentration was found to promote efficient protein refolding while reducing the prevalence of random coil structures (Supplementary Fig. 11 and Table 2). Consequently, a coagulation solution comprising 75% ethanol, pH 2.0, and 2% (w/v) H_2O_2 was validated for fiber preparation.

Subsequently, we investigated the mechanical tensile behavior of fibers across various protein weight ratios, as illustrated in Fig. 2e and Supplementary Fig. 12 and Table 3. The results reveal that despite exhibiting an enhanced tensile strain of 46.3 ± 9.4%, PKFs demonstrate inferior mechanical strength compared to those reported keratin-based fibers. This phenomenon could be attributed to the weak internal entanglement within PKFs, rendering it challenging to offset the loss of the rigid helix structure following refolding. With an increase in BSA content, the tensile strain of the fibers gradually rises from 46.3 ± 9.4% to 111.2 ± 23.8%, while the mechanical strength initially shows an ascending trend before descending. At a keratin/BSA ratio of 3:2, the UKBFs exhibit optimal mechanical performance, boasting a breaking strength of 119.2 ± 13.3 MPa and a toughness of 98.8 ± 10.8 MJ m⁻³ (Fig. 2f). We employed deconvolution analysis of the typical peaks in FTIR spectra (Supplementary Fig. 13 and Fig. 2g) located at 1650 cm⁻¹, 1620 cm⁻¹, and 1670 cm⁻¹ corresponding to α-helix, β-sheet, and disordered structures, respectively. As the proportion of BSA rises, the helical structures within the fibers gradually diminish, while β-sheet structures exhibit an initial rise followed by a decline. This behavior can be attributed to BSA's role in balancing the rigid secondary structures and chain entanglement within the fibers. Both keratin and BSA are rich in thiol groups, and the transition from solution to fiber involves the reorganization of disulfide bond networks, which govern their interactions and influence the distribution of secondary structures. Initially, the introduction of BSA promotes molecular chain entanglement and enhances interactions between keratin and BSA. During fiber formation, oxidative cross-linking occurs, which reduces the density of disulfide bonds that would otherwise form exclusively between keratin molecules. This dilution increases chain flexibility, enabling the stretching of helical structures into β-sheets[40], thereby increasing β-sheet content. However, as BSA content increases further, excessive entanglement begins to hinder these structural transitions, favoring the formation of random coils and reducing β-sheet content. This entanglement cannot compensate for the loss of keratin's rigid structure, leading to increased tensile strain but reduced tensile strength. Therefore, precisely controlling BSA content to regulate chain entanglement while maintaining adequate protein refolding capacity is essential for achieving an optimal balance between strength and toughness through the coordination of secondary structures.

Drawing-induced rearrangement of the molecular structure of DKBFs

Given that mechanical drawing is a critical procedure for improving tensile strength via molecular orientation and filament densification[1–3], we applied continuous stress to UKBFs to produce drawn keratin/BSA composite fibers (DKBFs). This procedure efficiently enhances fibril alignment while significantly maximizing the secondary structure transition from α-helix to β-sheet[24], as depicted in Fig. 3a. The morphology evolution observed in SEM images (Fig. 3b) shows a significant reduction in diameter from ~29 μm to ~12 μm as the drawing ratio (λ) increases from 1.0 to 3.0. Two-dimensional SAXS characterizes the protein molecular arrangement structure at various drawing ratios (Fig. 3c). As summarized in Fig. 3d, DKBFs exhibit an improved degree of order, with the orientation factor (f) increasing from 0.857 to 0.948. This is consistent with the enhanced birefringence observed upon drawing, as evidenced by POM images in Supplementary Figs. 14. The calculated β-sheet proportion significantly increases from 44.2% to 64.1% as the drawing ratio rises from 1.0 to 3.0 (Fig. 3e and Supplementary Fig. 15). In addition, Fig. 3f, g demonstrates a strong positive correlation between the tensile strength and drawing ratio (Supplementary Fig. 16 and Table 4). With an increase in the drawing ratio from 1.0 to 3.0, the tensile strength of DKBFs rises to 249.9 ± 8.3 MPa, marking a twofold enhancement compared to UKBFs. While a high drawing ratio improves the tensile strength of DKBFs, the drawing process consumes part of the deforming capacity of the protein molecular chain, reducing elongation at break to 40.8 ± 4.5%. Nonetheless, the toughness of DKBFs remains at 69.9 ± 10.0 MJ m⁻³ after mechanical drawing, demonstrating effective enhancement of protein chain entanglement in improving comprehensive mechanical properties. It is worth noting that the comprehensive mechanical properties of the current DKBFs are comparable to those of natural wool fibers (Supplementary Fig. 17) and even outperform those of various natural and artificial silk fibers, including degummed silk[46], regenerated silk fibers[47,48], recombinant spider silk fibers[49,50], and regenerated keratin fibers[24,27,30,34,51], as summarized in Fig. 3h and Supplementary Table 5.

Building on the strategy of chain entanglement enhancement and stretch-induced reinforcement to regulate the mechanical properties of composite fibers composed of fibrous and globular proteins, we extended our investigation to explore the applicability of this approach to other globular proteins. Considering that disulfide crosslinking of cysteine residues can significantly strengthen interactions between keratin and globular proteins, selecting globular proteins with an adequate number of cysteine residues is essential. Therefore, we chose three commonly used globular proteins—soy protein isolate (SPI), β-lactoglobulin (βLB), and ovalbumin (OVA)—for complexation with keratin. The results indicate that fibers composed of single proteins exhibit relatively low mechanical properties, with tensile strength below 40 MPa and toughness below 25 MJ m⁻³, which are inferior to those of pure BSA fibers (Supplementary Figs. 18 and Table 6). This discrepancy may be attributed to the intrinsic characteristics of different globular proteins, such as molecular weight and amino acid sequence. Nevertheless, after complexation with keratin
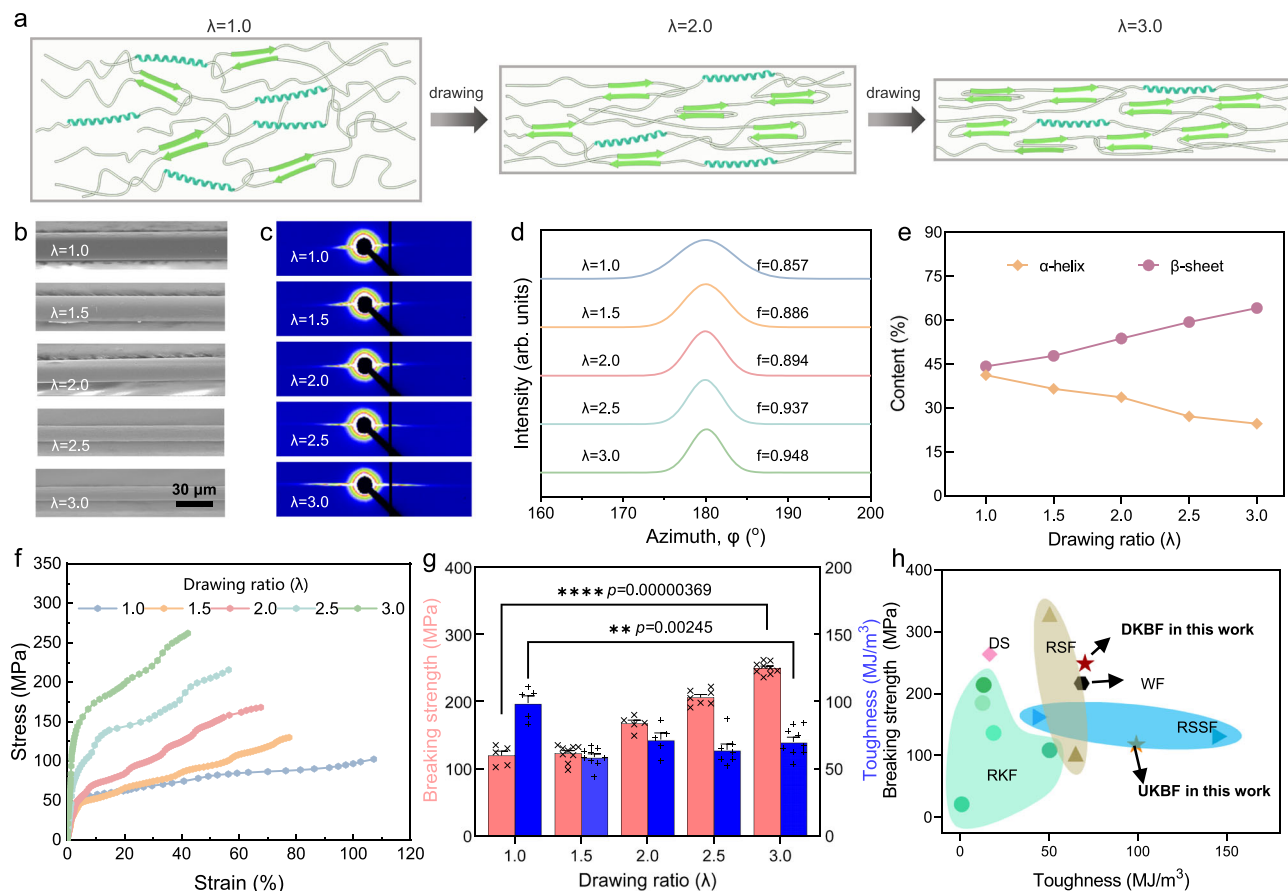
Fig. 3 | Drawing-induced secondary structure rearrangement and mechanical reinforcement of DKBFs. a A schematic depicts the reduction of fiber diameter and the transformation of β-sheet from α-helix during continuous mechanical drawing. **b** Representative SEM images of DKBFs under different drawing ratios exhibit a gradual decrease in fiber diameter ($n = 3$). **c** SAXS 2D patterns of DKBFs demonstrate an enhanced sharp orientation signal under varying drawing ratios from 1.0 to 3.0. **d** The azimuth (ϕ) plot of DKBFs under different drawing ratios reveals an increased orientation factor (f). **e** Changes in the secondary structure content of DKBFs with different drawing ratios are extracted from deconvolution analysis of the amide I/II region on the FTIR spectrum. **f** Representative stress–strain curves of DKBFs with different drawing ratios. **g** The breaking strength and toughness analysis of DKBFs with different drawing ratios. Data are presented as mean ± SD ($\lambda = 1.0$, $n = 5$; $\lambda = 1.5$, $n = 9$; $\lambda = 2.0$, $n = 5$; $\lambda = 2.5$, $n = 7$; $\lambda = 3.0$, $n = 9$). Statistical significance was determined by two-sample t-tests (OriginPro 2021). *ns* no significant difference; $*p < 0.05$; $**p < 0.01$; $***p < 0.001$; $****p < 0.0001$. **h** A comparison of output breaking stress and toughness between our UKBFs, DKBFs, and other natural and artificial protein fibers. Note: DS denotes degummed silk[46], RKF denotes regenerated keratin fiber[24,27,30,34,51], RSF denotes regenerated silk fiber[47,48], RSSF denotes recombinant spider silk fiber[49,50], WF denotes wool fiber. Source data are available in the Source Data file.

and subsequent tensile processing, the resulting fibers demonstrated significant improvements in mechanical properties, including strength, modulus, and toughness (Supplementary Fig. 19 and Table 7). These findings highlight the broad applicability and potential versatility of the proposed strategy.

Mechanical stability and redox-triggered reversible mechanics of DKBFs

Subsequently, the mechanical stability of the fibers was assessed through cyclic tensile testing. As depicted in Supplementary Fig. 20, when the tensile strain is set to 5% within the elastic deformation region, the fibers exhibit robust elastic recovery, with stress remaining constant. Upon increasing the strain to 20%, although notable irreversible deformation is observed in the tensile curve, the tensile stress can still be maintained at ~160 MPa. These results indicate the excellent mechanical stability of the fibers. Furthermore, thermal stability was evaluated using thermogravimetric analysis (TGA). The resulting DKBFs demonstrate a decomposition temperature close to ~250 °C in a nitrogen (N_2) atmosphere (Supplementary Fig. 21), closely resembling that of natural wool with its rigid scale layer protection (Supplementary Fig. 22), which could be attributed to the extensive disulfide crosslinking in DKBFs[24]. Considering the

high content of disulfides (S-S) present between fibrils providing mechanical strength for DKBFs, we explored the dynamical mechanical behaviors of DKBFs based on reversible cleavage of S-S bonds. As illustrated in Fig. 4a, treatment with DTT leads to the breakage and reduction of some disulfide bonds to thiol groups. Conversely, upon re-oxidation, the disulfide bonds are restored. Raman spectroscopy[52] (Fig. 4b, c) was employed to assess the relative S-S content (R_{ss}) around 510 cm^{-1}, revealing a decrease from 24.5% to 14.8% under DTT treatment, followed by a restoration to 28.9% after re-oxidation with H_2O_2, indicating the redox-responsive nature of DKBFs. The mechanical properties of DKBFs undergo dynamic changes due to the reversible cleavage and reconstruction of disulfide bonds. With an increase in DTT concentration from 10 mM to 30 mM, the tensile strength and toughness gradually decrease, resulting in a breaking strength of 82.8 ± 5.7 MPa and toughness of 25.5 ± 2.9 MJ m^{-3}, indicating an increasing disruption of disulfide bonds. However, after treating these mechanically weakened fibers with a 2% (w/v) H_2O_2 solution overnight, both the breaking strength and toughness are restored to their original levels (Fig. 4d, e, and Supplementary Figs. 23 and Table 8), thereby demonstrating the excellent mechanical reversibility of DKBFs. This highlights their potential application in redox-stimuli-responsive smart materials.
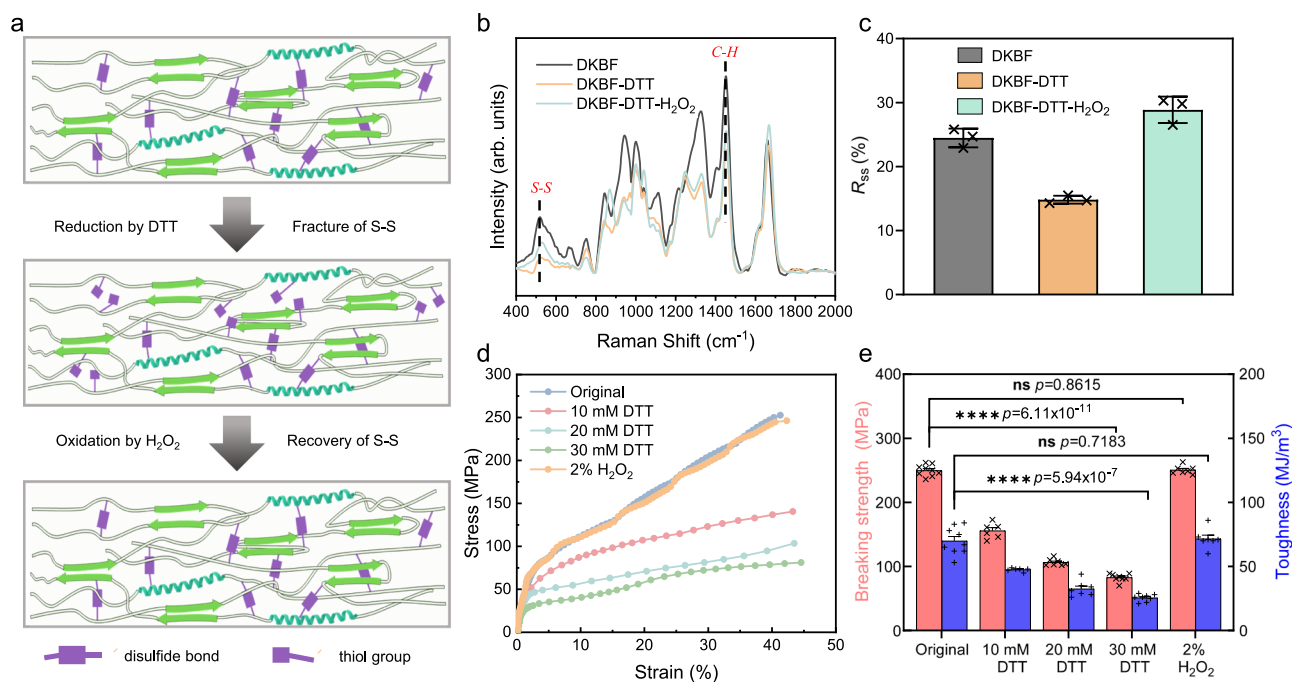
Fig. 4 | Redox-responsive mechanical behaviors of DKBFs. a. Schematic of the reversible fracture of S-S under reduction treatment by DTT and oxidation treatment by H_2O_2. **b, c** Raman spectra analyzing the change in disulfide bond content of DKBFs under different treatments. R_{ss} is the relative S-S content of peak areas of the S-S band (around 510 cm⁻¹) and C-H band (1450 cm⁻¹). Data are represented as mean ± SD ($n = 3$, three individual specimens were tested for each sample type). **d** Representative stress-strain curves of DKBFs under different redox treatments. **e** The breaking strength and toughness analysis of DKBFs under different redox treatments. Data are presented as mean ± SD (original, $n = 9$; 10 mM DTT, $n = 6$; 20 mM DTT, $n = 7$; 30 mM DTT, $n = 8$; 2% H_2O_2, $n = 7$). Statistical significance was determined by two-sample t-tests (OriginPro 2021). *ns* no significant difference; *$p < 0.05$; **$p < 0.01$; ***$p < 0.001$; ****$p < 0.0001$.

Hydration-induced mechanical behaviors of DKBFs

Generally, the β-sheets in DKBFs are kinetically stable owing to the presence of the H-bond network that hinders their reconversion into the more thermodynamically stable α-helixes. Therefore, a shape-memory cycle is allowed for the elaboration in which the H-bond network functions as a locking mechanism to ensure the persistence of the deformed shape (Fig. 5a)[40]. Upon hydration (Fig. 5b and Supplementary Movie 4), the DKBF (state A) bundle shrinks from approximately 15 cm to ~14 cm at state B, eventually stabilizing at about 13 cm in state B' after air drying. Subsequently, the contracted fiber bundle is re-hydrated and manually wet-stretched to a length of about 15 cm, then maintained under a load at room temperature until the fiber bundle dries (state C). Upon relaxation, no significant length change is observed between the stretched (state C) and relaxed forms (state A'). Notably, when the bundle is re-dried after being re-hydrated in state A', the bundle length returns to state B', indicating the shape memory cycle of DKBF bundles. Figure 5c, d and Supplementary Fig. 24 illustrate the changes in β-sheet and α-helix content in DKBF. The β-sheet content decreases from 64.1% to 34.8%, while the α-helix content increases from 24.6% to 42.5% upon hydration and dehydration. Upon subsequent re-stretching during rehydration and air drying, these structural shifts revert to their original proportions, thereby demonstrating the reversible transformation between β-sheets and α-helixes throughout the shape-memory cycle. Additionally, notable reversible changes in the birefringence of the filament bundle are observed during the stretching-hydration-drying cycles. Initially, the filament bundle contracts, accompanied by a decrease in birefringence, which is then restored to its original high-intensity state upon subsequent re-stretching and drying (Supplementary Fig. 25). This reversible transition is predominantly regulated by hydrogen bonding. Notably, the transition from β-sheet to α-helix involves the disruption of interchain hydrogen bonds in the β-sheet structure. This process is facilitated by the incorporation of water molecules, which establish new hydrogen bonds with the protein backbone, thereby stabilizing a more flexible and hydrated α-helix configuration. Under mechanical stretching, protein chains align, enabling the reformation of interchain hydrogen bonds and restoring the compact β-sheet structure as water molecules are expelled, completing the reversible cycle[30]. Leveraging this reversibility, the DKBF bundles could serve as artificial muscles and water-sensitive fabric actuators.

In addition to their excellent mechanical properties, DKBFs exhibit good biocompatibility and biodegradability, as their primary components are natural proteins, and their ultimate degradation products are amino acids. Cell cultures of L929 cells with DKBFs show healthy growth after 24 h, and it is observed that the cells can adhere to the fiber surface (Supplementary Figs. 26). In vitro degradation of DKBFs in elastase shows that 5 mg of DKBFs in 1 mL of elastase (0.2 mg mL⁻¹) can be gradually degraded over 30 days (Supplementary Figs. 27). To explore the potential biomedical applications of DKBFs, we further twisted and wove them into bundles, as shown in Fig. 5e. In the hydrated state, the woven DKBF bundle demonstrates a breaking strength of 78.6 ± 5.9 MPa and a modulus of 13.5 ± 2.9 MPa, with a fracture strain exceeding 200%, displaying a J-shaped stress-strain curve[53] (Fig. 5f and Supplementary Fig. 28). This phenomenon could be attributed to water's plasticization of the molecular chains, facilitating the conversion of β-sheets into stretchable α-helixes in the hydrated state[40]. Concurrently, the twisting and weaving processes may offer additional deformation potential[54], ultimately resulting in characteristic nonlinear tensile curves. Additionally, the load–unload cycles of the bundles at different set strains were conducted to characterize mechanical stability in the hydrated state (Fig. 5g), demonstrating excellent deformation recovery even at a set strain of 50%. The comprehensive mechanical performance, biocompatibility, and degradability make DKBFs promising load-bearing materials for biomedical applications[55].
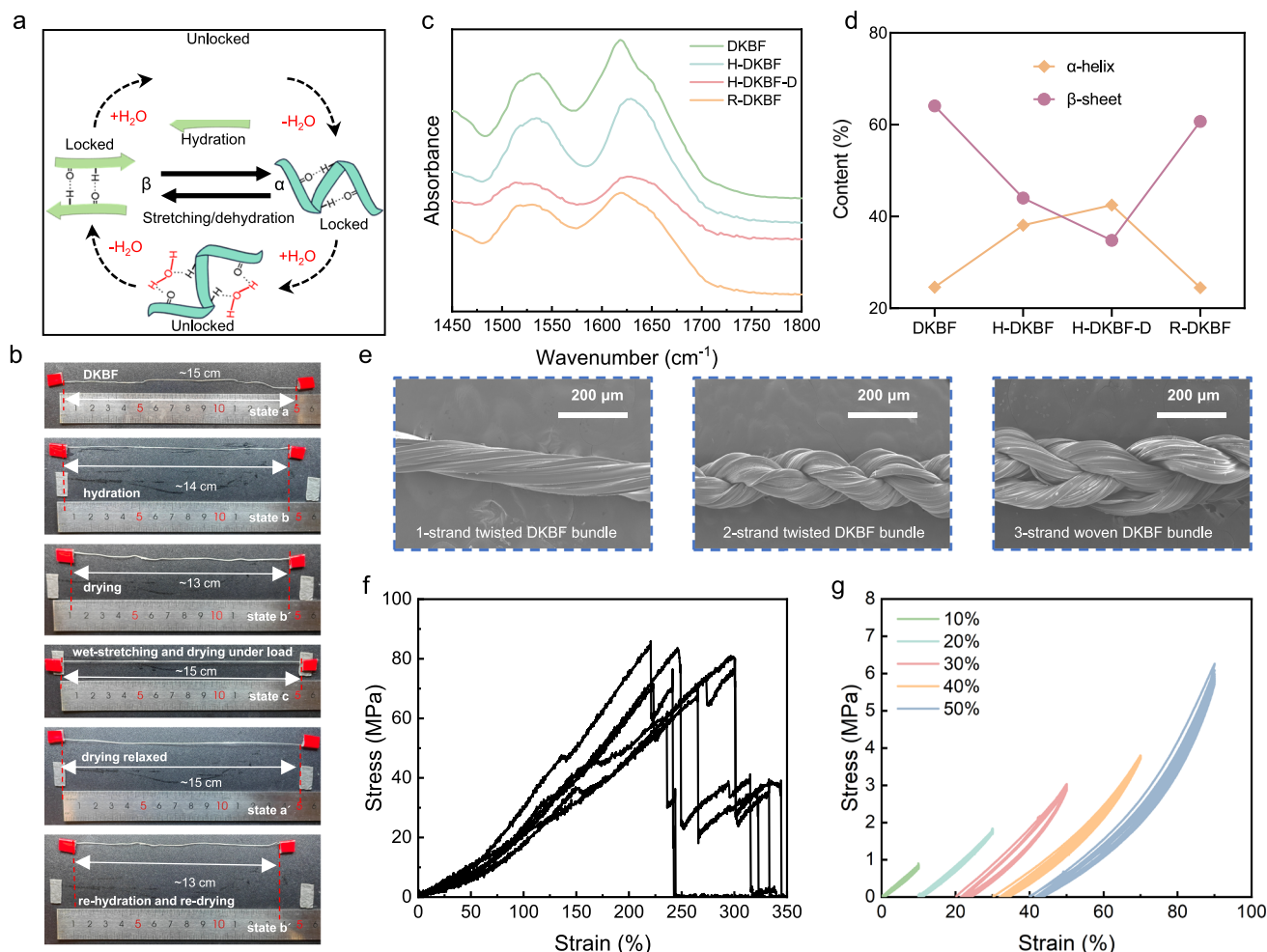
Fig. 5 | Hydration-regulated mechanical behaviors of DKBFs. a Schematic illustrating the reversible transformation between folding and helical structures during hydration, stretching, and dehydration treatment. **b** Images show reversible length changes of the DKBF bundle. States of DKBF bundle during the process: A, DKBF bundle; B, bundle hydration; B', DKBF bundle hydration and drying; C, DKBF bundle wet-stretching and drying under load; A', DKBF bundle drying relaxed after stretching. **c**, **d** Changes in secondary structure content of DKBF, hydrated DKBFs (H-DKBF), hydrated and dried DKBFs (H-DKBF-D), and re-stretched DKBF (R-DKBF) as extracted from the deconvolution analysis of the amide I/II region on FTIR spectrum. **e** Representative SEM images of twisted and woven DKBF bundles ($n = 3$). **f** Tensile curves of hydrated 3-strand woven DKBF bundle. **g** Cyclic tensile curves of hydrated 3-strand woven DKBF bundles under different set strains (10%, 20%, 30%, 40%, and 50%). The curves are offset by a 10% strain for better visualization. Source data are available in the Source Data file.

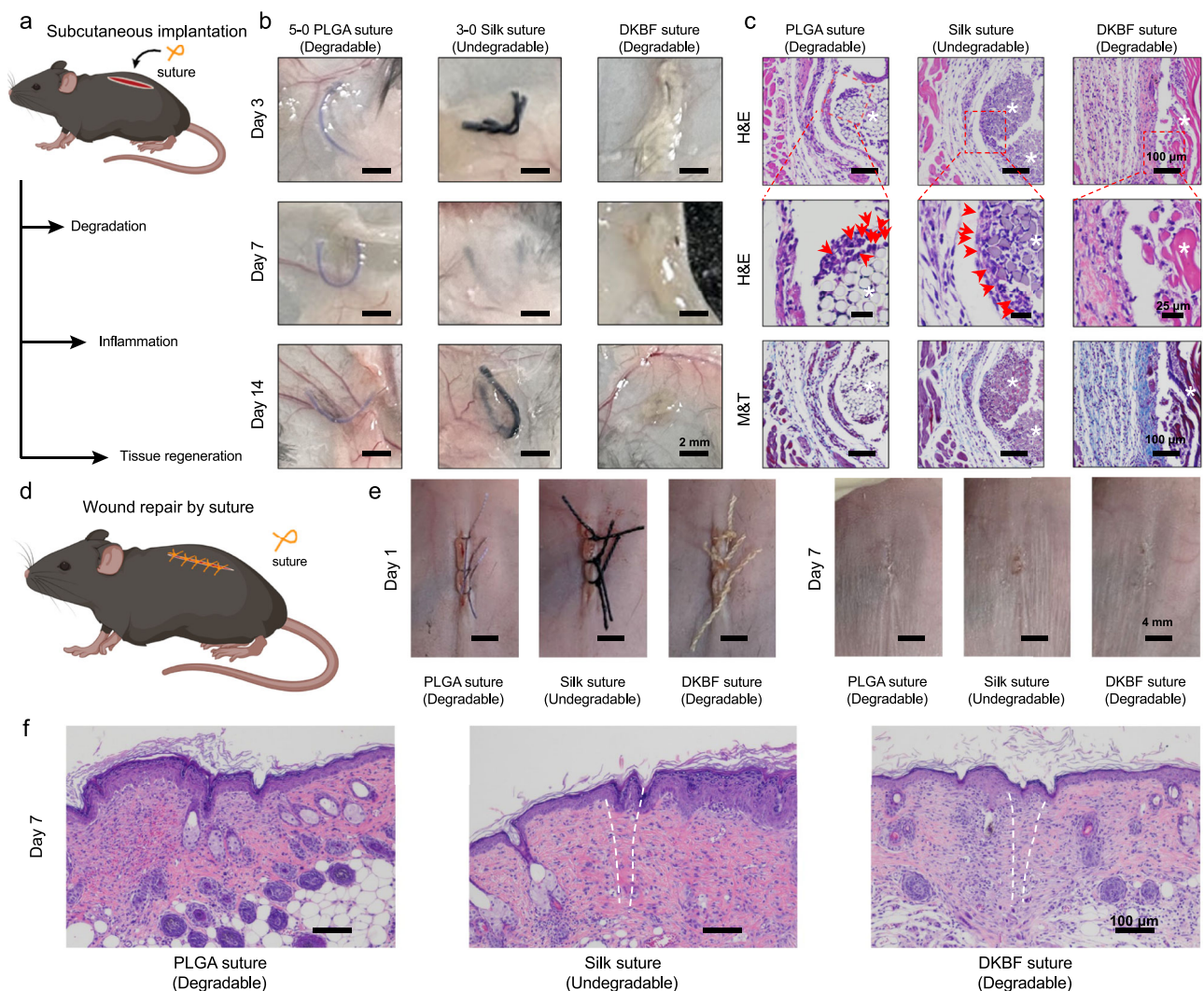## In vivo immunocompatibility and wound closure of DKBF suture

In addition to their excellent mechanical and biological properties, the relatively low production cost of DKBFs, at just 0.0011 USD m^{-1} (Supplementary Table 9), makes them particularly well-suited for surgical sutures. To further assess their in vivo performance, including degradability, immunocompatibility, and wound healing potential, DKBF sutures were implanted subcutaneously in C57BL/6 mice (Fig. 6a). Absorbable PLGA sutures and non-absorbable silk sutures were employed as controls. No notable degradation is observed for either PLGA or silk sutures during the 2-week period. However, the DKBF sutures exhibit significant biodegradability, approaching complete degradation by day 14 (Fig. 6b). Histological staining (H&E) images reveal that PLGA and silk sutures elicit a strong inflammatory response by day 7, whereas the DKBF sutures induce negligible inflammation, significantly superior to the other sutures. This is evidenced by increased cell infiltration into the interfilament spacings of PLGA and silk sutures over time, along with the presence of foreign body giant cells and proinflammatory eosinophils near the suture filaments. For the DKBF sutures, no giant cells, neutrophils, or macrophages were observed by day 7. M&T sections show that there is no significant tissue regeneration around the PLGA and silk sutures,

whereas loose collagen fibers appear around the DKBF suture, indicating its ability to promote tissue repair effectively (Fig. 6c). To demonstrate the use of DKBF sutures for wound closure, we further evaluated the wound healing of dorsal full-thickness skin incisions closed using PLGA, silk, or DKBF sutures in a mouse model (Fig. 6d). Macroscopic assessment of the wounds on day 7 shows that all sutures exhibit good wound closure capability, with no signs of infection (Fig. 6e). Histological assessment confirmed complete healing of all incisional wounds by primary intention, with minimal inflammation and fibrosis (Fig. 6f).

Discussion

In summary, we have engineered a keratin/BSA composite fiber with both high strength and toughness through enhanced protein chain entanglement, without the addition of chemical crosslinkers. The synergistic interaction between keratin and BSA has effectively tailored the mechanical properties of the composite fibers. The resulting DKBFs demonstrate a well-balanced mechanical performance, featuring a breaking strength of ~250 MPa and a toughness of around 70 MJ m^{-3}, which matches or exceeds that of natural or artificial protein fibers. DKBFs can be intricately twisted and woven into bundles,

Fig. 6 | In vivo biocompatibility and wound closure of PLGA, silk, and DKBF sutures. a Schematic illustration of the subcutaneous implantation of sutures in C57BL/6 mice. Degradability was assessed on days 3, 7, and 14, while inflammation and tissue regeneration were evaluated on day 7. **b** Digital photographs of the sutures at various time points following subcutaneous implantation. **c** Hematoxylin and eosin (H&E) and Masson's trichrome (M&T) stained histological sections of excised tissues on day 7 ($n = 3$ mice per group). Asterisks (*) in the section images indicate the original locations of the implants. Red arrows in the section images point to the foreign body giant cells. **d** Schematic illustration of incision wounds closed with PLGA, silk, and DKBF sutures. **e** Images of wounds stitched with PLGA, silk, and DKBF sutures on day 1 and day 7. **f** H&E staining of wound tissues stitched with different sutures on day 7 ($n = 3$ mice per group). The dotted lines in the section images mark the location of the healed wound. Note: **a** and **d** are created in BioRender. Ji, J. (2025) https://BioRender.com/w03w579.

exhibiting high mechanical strength and stability under hydrated conditions. In addition, due to their degradability and immuno-compatibility, sutures made of DKBFs demonstrate good wound closure capability, with significantly less inflammations compared with PLGA and silk sutures. We envision that the robust and resilient DKBF could inspire valuable insights for innovative bio-regenerated fiber manufacturing and stimuli-responsive and biomedical applications.

Methods

Wet spinning of keratin/BSA composite fibers

First, a denaturant solvent was prepared using 8 M urea and 0.1 M DTT. Keratin powder extracted from Angora Wool was dissolved in the denaturant solvent at 90 °C, while BSA was dissolved at room temperature. Both the keratin and BSA solutions were degassed by centrifugation, resulting in a final concentration of 200 mg mL^{-1}. The protein composite spinning dope was then prepared by mixing the solutions in different weight ratios. Afterward, the protein composite spinning dope was extruded by a syringe pump at a flow rate of 10 μL min^{-1} through a needle with an inner diameter of 210 μm and a length of 75 mm into a coagulation bath containing 2% (w/v) H$_2$O$_2$ and 75% v/v ethanol at a pH of 2.0. Keratin filaments were collected at a rate of 1.6 m min^{-1}. The drawn keratin/BSA composite fibers (DKBFs) were obtained under different drawing ratios ($\lambda = 1.0$, 1.5, 2.0, 2.5, and 3.0) based on the initial collection rate of 1.6 m min^{-1}. Other spherical proteins, including SPI, βLB, and OVA, were prepared using the same procedure as BSA for the fabrication of composite fibers with keratin. The resulting fibers were then dried under ambient conditions (room temperature: ~25 °C, relative humidity: 50–60%).

Preparation of DKBF bundles

Fibers were collected into a bundle with a diameter of ~100 μm and a length of 15 cm. The bundle was twisted using a motor at 200 rpm for 2 min to obtain a 1-strand twisted DKBF bundle. Two 1-strand bundles, twisted in opposite directions, were combined to form a 2-strand twisted DKBF bundle. Subsequently, three 1-strand bundles were then braided together to create a 3-strand woven DKBF bundle.

Preparation of sutures

For suture preparation, a fiber bundle with a diameter of 200 µm and a length of 15 cm was twisted and then combined in reverse to form a suture, resulting in a macroscopic diameter of ~400 µm.

Mechanical tests

Tensile testing of the single fiber was performed using a testing machine (Discovery DMA 850, TA-waters) equipped with an 18 N sensor and pneumatic grip. Before the test, the fibers were affixed to a hollow paper frame (5 × 5 mm) and conditioned at room temperature (~25 °C) and 60% relative humidity for 24 h. The testing was conducted in Rate Control-Stress Ramp mode with a ramp rate of 0.1 N min⁻¹. Tensile testing of DKBF bundles was carried out using a Computerized Electronic Universal Testing Machine (Shenzhen Suns Technology Stock Co. Ltd.).

Physicochemical characterization

The viscosity measurements of the spinning dope were performed on a rotational rheometer (Hacke MARS, Thermo Fisher) with 25 mm rotor under 25 °C. The shear rate was from 0.01 to 1000 s⁻¹. The consistency coefficient (K) and non-Newtonian exponent (n) were determined as expressed in equation: $\tau = K\gamma^n$, where γ denotes the shear rate and τ is the shear stress[45]. The secondary structures of prepared fibers were analyzed by an IR spectrophotometer (Nicolet iS20, Thermo Fisher Scientific). The deconvolution, baseline-correction, and smoothing of spectra were performed using Origin 2021 software. The Fit Peaks (Pro) modes of the peak analyzer tool and the Gaussian Peak Function were utilized for the peak deconvolution. The content of disulfide bonds within prepared fibers was analyzed by a Raman Spectrometer (LABRAM HR Evolution, HORIBA Jobin Yvon). The excitation wavelength was 633 nm. The normalization of Raman spectral data was based on the C-H band due to its large peak area and not affected by chemical treatment. The disulfide bond content in fibers was calculated according to the formula: $R_{ss} = \frac{S_{510}}{S_{1450}}$, where S_{510} is the peak area of S-S band (470-560 cm⁻¹), while S_{1450} is C-H band peak area (1430–1500 cm⁻¹).

Molecular dynamic (MD) simulations

To investigate the structural differences of proteins in urea aqueous solvent conditions with various structural systems, MD simulations were performed using the Gromacs 2021.5 open-source software package. The simulation systems were set up in a closed environment, with all systems maintained at a pressure of 1 bar (atmospheric pressure). The sequences of BSA (UniProt ID: P02769, ALBU_BOVIN) and keratin (UniProt ID: P25690, K1M2_SHEEP) can be obtained from the https://www.uniprot.org/ (supplementary Table 10). The temperature of the BSA system was set to 300 K, while the temperature of the keratin system was set to 363 K, with shear force applied to both, simulating the actual dissolution temperature and stirring shear forces. The mixed system was simulated at 300 K. Periodic boundary conditions were applied with the protein centered within the simulation box, ensuring that the minimum distance between the protein's edge and the box edge was set to 5.0 nm. The receptor structure topology files were converted into GROMACS-compatible formats using the pdb2gmx tool, with the AMBERff14SB force field used for the simulations. The TIP3P model was employed for water molecules. After constructing the initial system, energy minimization was performed on all atoms using the steepest descent method. After fixing the protein positions, a 1000 ps constant number of particles, volume, and temperature (NVT) equilibrium simulation was first performed, followed by a 1000 ps constant number of particles, pressure, and temperature (NPT) equilibrium simulation. After NVT and NPT equilibration, both the wild-type and mutant systems were simulated for 100 ns in production dynamics, with a simulation step of 2 fs. The bond lengths were constrained using a linear constraint

solver, and long-range electrostatic interactions were calculated using the Particle Mesh Ewald method. Once all simulations were completed, structural analysis, including the calculation of the Rg and root mean square deviation, was performed using the GROMACS gmx module. The snapshots of the protein structures after unfolding were captured at 75 ns for BSA, 40 ns for keratin, and 100 ns for the composite system, respectively. These time points were determined based on the results of the actual SAXS measurements of the Rg.

Animal work

All mouse experiments were conducted in strict accordance with relevant regulations, and the research protocols were approved by the Lab of Animal Experimental Ethical Inspection of Dr. Can Biotechnology (Zhejiang) Co., Ltd (Approval number: DRK2023150287). Female mice of the wild-type (WT) C57BL/6 strain, aged 6 to 8 weeks, were obtained from the animal facility of the Zhejiang Academy of Medical Sciences. All animals were maintained under controlled environmental conditions with a temperature range of 18–29 °C, relative humidity of 45–55%, and ventilation rate of 6–15 air changes per hour. The animals were provided with a standard laboratory diet and housed under a 12-h light/dark cycle.

For subcutaneous implantation procedures in mice, the sutures were washed with PBS buffer and sterilized via UV irradiation for 30 min and implanted subcutaneously in C57BL/6 female mice. The implantation process was meticulously conducted as follows: mice were anesthetized using 3% isoflurane in oxygen, their skin was carefully shaved, and then disinfected with iodine. A longitudinal incision of approximately 6 mm was made on the dorsal surface using surgical scissors. Subsequently, the incisions were closed with PLGA, silk, and DKBF sutures, respectively. The mice were monitored until they recovered from anesthesia and maintained for 3, 7, and 14 days. They exhibited normal growth with no signs of discomfort after implantation, and no body weight loss was observed throughout the experiment.

For the incision wound model in mice, the sutures were sterilized via UV irradiation for 30 min. The procedure was meticulously conducted as follows: mice were anesthetized using 3% isoflurane in oxygen, their skin was carefully shaved, and disinfected with iodine. A longitudinal incision of ~8 mm was made on the dorsal surface using surgical scissors to provide access to the subcutaneous space. Subcutaneous pockets about 0.5 cm away from the incision were created with blunt forceps for the implantation of the sutures. After implantation, the incisions were closed with 5-0 taper-tipped PGA absorbable sutures. The mice were monitored until recovery from anesthesia and maintained for 7 days. They exhibited normal growth with no signs of discomfort after implantation, and no body weight loss was observed throughout the experiment. At specific time intervals, mice were sacrificed, and the suture samples, along with adjacent tissues, were photographed, excised, and collected. These explanted samples were fixed in a 10% formaldehyde solution for histological examination.

Statistics and reproducibility

Details regarding sample sizes and the appropriate statistical tests employed are provided in the figure captions. Data are presented as means ± standard deviation. Significance testing was performed using two-sample t-tests via OriginPro 2021 software. It should be noted that due to the mechanical testing procedure, which involves clamping fibers with paper clips before conducting tests using Dynamic Mechanical Analysis, some tests may fail due to sample preparation issues. Therefore, the actual sample sizes achieved are specified in the corresponding figure captions. All in vivo experimental results are derived from three independent experiments to ensure the reproducibility of the findings.

Reporting summary

Further information on research design is available in the Nature Portfolio Reporting Summary linked to this article.

Data availability

Source data for figures in the article are provided with this paper. All data underlying this study are available from the corresponding author upon request. Source data are provided with this paper.

References

1. Su, J. et al. Engineering high strength and super-toughness of unfolded structural proteins and their extraordinary anti-adhesion performance for abdominal hernia repair. *Adv. Mater.* **34**, 2200842 (2022).
2. Sun, J. et al. Protein fibers with self-recoverable mechanical properties via dynamic imine chemistry. *Nat. Commun.* **14**, 5348 (2023).
3. He, H. et al. Mechanically strong globular-protein-based fibers obtained using a microfluidic spinning technique. *Angew. Chem. Int. Ed.* **59**, 4344–4348 (2020).
4. Ma, C. et al. Ultra-strong bio-glue from genetically engineered polypeptides. *Nat. Commun.* **12**, 3613 (2021).
5. Fu, C. et al. Protein-based bioactive coatings: from nanoarchitectonics to applications. *Chem. Soc. Rev.* **53**, 1514–1551 (2024).
6. Li, H., Kong, N., Laver, B. & Liu, J. Hydrogels constructed from engineered proteins. *Small* **12**, 973–987 (2016).
7. Shi, C. et al. Flexible and insoluble artificial synapses based on chemical cross-linked wool keratin. *Adv. Funct. Mater.* **30**, 2002882 (2020).
8. Tu, H. et al. Programing performance of wool keratin and silk fibroin composite materials by mesoscopic molecular network reconstruction. *Adv. Funct. Mater.* **26**, 9032–9043 (2016).
9. Gomes, S., Leonor, I. B., Mano, J. F., Reis, R. L. & Kaplan, D. L. Natural and genetically engineered proteins for tissue engineering. *Prog. Mater. Sci.* **37**, 1–17 (2012).
10. Pan, L. et al. A supertough electro-tendon based on spider silk composites. *Nat. Commun.* **11**, 1332 (2020).
11. Xiao, Y. et al. Strong and tough biofibers designed by dual cross-linking for sutures. *Adv. Funct. Mater.* **34**, 2313131 (2024).
12. Wang, M. et al. Modular protein fibers with outstanding high-strength and acid-resistance performance mediated by copper ion binding and imine networking. *Adv. Mater.* **36**, 2400544 (2024).
13. Chen, M., Fu, X., Chen, Z., Liu, J. & Zhong, W. H. Protein-engineered functional materials for bioelectronics. *Adv. Funct. Mater.* **31**, 2006744 (2021).
14. Ritchie, R. O. The conflicts between strength and toughness. *Nat. Mater.* **10**, 817–822 (2011).
15. Yarger, J. L., Cherry, B. R. & van der Vaart, A. Uncovering the structure–function relationship in spider silk. *Nat. Rev. Mater.* **3**, 18008 (2018).
16. Keten, S., Xu, Z., Ihle, B. & Buehler, M. J. Nanoconfinement controls stiffness, strength and mechanical toughness of β-sheet crystals in silk. *Nat. Mater.* **9**, 359–367 (2010).
17. Altman, G. H. et al. Silk-based biomaterials. *Biomaterials* **24**, 401–416 (2003).
18. Li, Y. et al. Advances, challenges, and prospects for surgical suture materials. *Acta Biomater.* **168**, 78–112 (2023).
19. Li, Y. et al. Bioinspired and mechanically strong fibers based on engineered non-spider chimeric proteins. *Angew. Chem. Int. Ed.* **59**, 8148–8152 (2020).
20. Zhang, J. et al. Robust biological fibers Based on widely available proteins: facile fabrication and suturing application. *Small* **16**, 1907598 (2020).
21. Beauchamp, R. O. et al. A critical review of the toxicology of glutaraldehyde. *Crit. Rev. Toxicol.* **22**, 143–174 (1992).
22. Reddy, N., Reddy, R. & Jiang, Q. Crosslinking biopolymers for biomedical applications. *Trends Biotechnol.* **33**, 362–369 (2015).
23. Feroz, S., Muhammad, N., Ratnayake, J. & Dias, G. Keratin-based materials for biomedical applications. *Bioact. Mater.* **5**, 496–509 (2020).
24. Zhu, J. et al. Reinforced wool keratin fibers via dithiol chain re-bonding. *Adv. Funct. Mater.* **33**, 2213644 (2023).
25. Cao, G., Rong, M. Z. & Zhang, M. Q. Continuous high-content keratin fibers with balanced properties derived from wool waste. *ACS Sustain. Chem. Eng.* **8**, 18148–18156 (2020).
26. Mu, B., Yu, X. & Yang, Y. Sustainable and green process for recycling waste wool textiles into high-quality protein fibers on a pilot scale. *Resour. Conserv. Recy.* **198**, 107190 (2023).
27. Sun, J. et al. Bioinspired processing of keratin into upcycled fibers through pH-induced coacervation. *ACS Sustain. Chem. Eng.* **11**, 1985–1994 (2023).
28. Sun, J., Monreal Santiago, G., Zhou, W., Portale, G. & Kamperman, M. Water-processable, stretchable, and ion-conducting coacervate fibers from keratin associations with polyelectrolytes. *ACS Sustain. Chem. Eng.* **10**, 15968–15977 (2022).
29. Katoh, K., Shibayama, M., Tanabe, T. & Yamauchi, K. Preparation and properties of keratin–poly(vinyl alcohol) blend fiber. *J. Appl. Polym. Sci.* **91**, 756–762 (2004).
30. Xu, X. et al. Reconstructed hierarchically structured keratin fibers with shape-memory features based on reversible secondary-structure transformation. *Adv. Mater.* **35**, 2304725 (2023).
31. Qin, C. et al. Insight into the keratin ratio effect of the keratin/cellulose composite fiber. *ACS Appl. Polym. Mater.* **6**, 265–276 (2024).
32. Fang, W., Fan, R., Aranko, A. S., Hummel, M. & Sixta, H. Upcycling of keratin wastes in sustainable textile fiber applications. *ACS Sustain. Chem. Eng.* **11**, 14807–14815 (2023).
33. Wei, W. et al. Preparation and characterization of protein/viscose fiber and its action in self-heating. *J. Appl. Polym. Sci.* **136**, 47146 (2019).
34. Zhang, L. et al. Ultra-strong regenerated wool keratin fibers regulating via keratin conformational transition. *Adv. Funct. Mater.* **33**, 2301447 (2023).
35. Allen, G. The physics of rubber elasticity (third edition): L. R. G. Treloar Clarendon Press, Oxford, 1975, pp 310, £14.00. *Polymer* **17**, 360 (1976).
36. Fu, L. et al. Cartilage-like protein hydrogels engineered via entanglement. *Nature* **618**, 740–747 (2023).
37. Kong, D.-C. et al. Control of polymer properties by entanglement: a review. *Macromol. Mater. Eng.* **306**, 2100536 (2021).
38. Kamiyama, Y. et al. Highly stretchable and self-healable polymer gels from physical entanglements of ultrahigh–molecular weight polymers. *Sci. Adv.* **8**, eadd0226 (2022).
39. Kim, J., Zhang, G., Shi, M. & Suo, Z. Fracture, fatigue, and friction of polymers in which entanglements greatly outnumber cross-links. *Science* **374**, 212–216 (2021).
40. Cera, L. et al. A bioinspired and hierarchically structured shape-memory material. *Nat. Mater.* **20**, 242–249 (2021).
41. Betz, S. F. Disulfide bonds and the stability of globular proteins. *Protein Sci.* **2**, 1551–1558 (1993).
42. Liu, Y. et al. Synthesis of robust underwater glues from common proteins via unfolding-aggregating strategy. *Nat. Commun.* **14**, 5145 (2023).
43. Fioroni, M., Diaz, M. D., Burger, K. & Berger, S. Solvation phenomena of a tetrapeptide in water/trifluoroethanol and water/ethanol mixtures: a diffusion NMR, intermolecular NOE, and molecular dynamics study. *J. Am. Chem. Soc.* **124**, 7737–7744 (2002).
44. Kumaran, R. & Ramamurthy, P. Denaturation mechanism of BSA by urea derivatives: evidence for hydrogen-bonding mode from fluorescence tools. *J. Fluoresc.* **21**, 1499–1508 (2011).

45. Chhabra, R. P. & Richardson, J. F. *Non-Newtonian Flow and Applied Rheology: Engineering Applications*. (Butterworth-Heinemann, 2011).

46. Lu, L., Fan, S., Geng, L., Yao, X. & Zhang, Y. Low-loss light-guiding, strong silk generated by a bioinspired microfluidic chip. *Chem. Eng. J.* **405**, 126793 (2021).

47. Xu, X. et al. Biomimetic design of hydration-responsive silk fibers and their role in actuators and self-modulated textiles. *Adv. Funct. Mater.* **34**, 2401732 (2024).

48. Madurga, R. et al. Production of high-performance bioinspired silk fibers by straining flow spinning. *Biomacromolecules* **18**, 1127–1133 (2017).

49. Andersson, M. et al. Biomimetic spinning of artificial spider silk from a chimeric minispidroin. *Nat. Chem. Biol.* **13**, 262–264 (2017).

50. Arndt, T. et al. Engineered spider silk proteins for biomimetic spinning of fibers with toughness equal to dragline silks. *Adv. Funct. Mater.* **32**, 2200986 (2022).

51. Mu, B., Hassan, F. & Yang, Y. Controlled assembly of secondary keratin structures for continuous and scalable production of tough fibers from chicken feathers. *Green. Chem.* **22**, 1726–1734 (2020).

52. Wang, C. H., Huang, C. C., Lin, L. L. & Chen, W. The effect of disulfide bonds on protein folding, unfolding, and misfolding investigated by FT–Raman spectroscopy. *J. Raman Spectrosc.* **47**, 940–947 (2016).

53. Brennan, D. A. et al. Mechanical considerations for electrospun nanofibers in tendon and ligament repair. *Adv. Funct. Mater.* **7**, 1701277 (2018).

54. Laranjeira, M., Domingues, R. M. A., Costa-Almeida, R., Reis, R. L. & Gomes, M. E. 3D mimicry of native-tissue-fiber architecture guides tendon-derived cells and adipose stem cells into artificial tendon constructs. *Small* **13**, 1700689 (2017).

55. Chanda, A. & Singh, G. Introduction to Human Tissues. In: *Mechanical Properties of Human Tissues* (eds. Chanda A., Singh G.). Springer Nature Singapore (2023).

Acknowledgements

Author contributions

Conceptualization, Haonan He, Xianchi Zhou, Peng Zhang, and Jian Ji; Methodology, Haonan He, Xianchi Zhou, Peng Zhang, and Jian Ji; Investigation, Haonan He, Xianchi Zhou, Yuxian Lai, Rouye Wang, Hongye Hao, and Xintian Shen; Writing–Original Draft, Haonan He, Xianchi Zhou; Writing–Review & Editing, Haonan He, Xianchi Zhou, and Peng Zhang; Funding Acquisition, Peng Zhang, Haonan He and Jian Ji; Supervision, Peng Zhang and Jian Ji.

Competing interests

J.J., P.Z., and H.H. are inventors of a patent related to this work filed by Zhejiang University (ZL 202411071835.6), the remaining authors declare no competing interest.

Declaration of generative AI and AI-assisted technologies in the writing process

During the preparation of this work, the author(s) used ChatGPT in order to improve the language and readability of the manuscript. After using this tool or service, the author(s) reviewed and edited the content as needed and take(s) full responsibility for the content of the publication.

Additional information

Supplementary information The online version contains supplementary material available at https://doi.org/10.1038/s41467-025-58171-0.

Correspondence and requests for materials should be addressed to Peng Zhang or Jian Ji.

Peer review information *Nature Communications* thanks Yuan Cheng, Yuanlong Shao, Ryota Tamate and the other, anonymous, reviewer(s) for their contribution to the peer review of this work. A peer review file is available.

Reprints and permissions information is available at http://www.nature.com/reprints

Publisher's note Springer Nature remains neutral with regard to jurisdictional claims in published maps and institutional affiliations.